HHS Public Access

Author manuscript

Phys Med Biol. Author manuscript; available in PMC 2020 June 20.

Published in final edited form as:

Phys Med Biol. ; 64(12): 125019. doi:10.1088/1361-6560/ab1f2b.

Inversion of displacement fields to quantify the magnetic particle distribution in homogeneous elastic media from magnetomotive ultrasound

Diwash Thapa[1], **Benjamin E Levy**[1], **Daniel L Marks**[3], **Amy L Oldenburg**[1,2,4]

[1]Department of Physics and Astronomy, University of North Carolina at Chapel Hill, Chapel Hill, NC 27599, United States of America

[2]Biomedical Research Imaging Center, University of North Carolina at Chapel Hill, Chapel Hill, NC 27599, United States of America

[3]Department of Electrical and Computer Engineering, Duke University, Durham, NC 27708, United States of America

Abstract

Magnetomotive ultrasound (MMUS) contrasts superparamagnetic iron-oxide nanoparticles (SPIOs) that undergo submicrometer-scale displacements in response to a magnetic gradient force applied to an imaging sample. Typically, MMUS signals are defined in a way that is proportional to the medium displacement, rendering an indirect measure of the density distribution of SPIOs embedded within. Displacement-based MMUS, however, suffers from 'halo effects' that extend into regions without SPIOs due to their inherent mechanical coupling with the medium. To reduce such effects and to provide a more accurate representation of the SPIO density distribution, we propose a model-based inversion of MMUS displacement fields by reconstructing the body force distribution. Displacement fields are modelled using the static Navier-Cauchy equation for linear, homogeneous, and isotropic media, and the body force fields are, in turn, reconstructed by minimizing a regularized least-squares error functional between the modelled and the measured displacement fields. This reconstruction, when performed on displacement fields of two tissue-mimicking phantoms with cuboidal SPIO-laden inclusions, improved the range of errors in measured heights and widths of the inclusions from 54%–282% pre-inversion to-15%–20%. Likewise, the post-inversion contrast to noise ratios (CNRs) of the images were significantly larger than displacement-derived CNRs alone ($p = 0.0078$, Wilcoxon signed rank test). Qualitatively, it was found that inversion ameliorates halo effects and increases overall detectability of the inclusion. These findings highlight the utility of model-based inversion as a tool for both signal processing and accurate characterization of the number density distribution of SPIOs in magnetomotive imaging.

Keywords

magnetomotive ultrasound; superparamagnetic iron oxides; contrast-enhanced imaging; inverse problem; elastostatics; Navier-Cauchy equation; regularized conjugate gradient

[4]Author to whom any correspondence should be addressed. aold@physics.unc.edu.

Introduction

Magnetomotive imaging is a contrast-enhanced imaging technique that uses magnetic nanoparticles (MNPs) as contrast agents and an externally applied, temporally modulated, magnetic field that creates a time-varying magnetic gradient force on the MNPs. The premise of image formation in magnetomotive imaging is that MNPs pulled by gradient forces induce displacements in the surrounding media to which they are mechanically coupled. These displacements are consistent with the time variation of the input magnetic field, providing rejection of motion artifacts and high specificity to the presence of the MNPs. The need to rapidly and sensitively measure displacement fields to perform magnetomotive imaging is met by interferometric imaging modalities such as optical coherence tomography (OCT) and ultrasound (US) imaging. Magnetomotive optical coherence tomography (MMOCT) was first demonstrated by Oldenburg *et al* (2005a), followed by the implementation of magnetomotive ultrasound (MMUS) by Oh *et al* in 2006. One advantage of magnetomotive imaging is that the contrast agents may be comprised of biocompatible iron-oxides, such as superparamagnetic iron-oxide (SPIO) nanoparticles originally developed for magnetic resonance imaging (MRI). This is favorable in biomedical applications, such as MMOCT for detection of vulnerable atherosclerotic plaques (Kim *et al* 2016), multimodal MMOCT and MRI of tumors *in vivo* (John *et al* 2010), MMUS for detection of thrombosis (Pope *et al* 2013, Levy *et al* 2018), and MMUS to detect breast cancer metastasis (Evertsson *et al* 2014, 2017). Importantly, SPIOs may be used in magnetomotive imaging even though they do not directly provide contrast in OCT (light scattering) or ultrasound (acoustic scattering), because the deformation of light- or acoustically-scattering tissue is detected. However, this has the consequence of magnetomotive images exhibiting signals beyond the boundaries of where SPIOs have accumulated due to mechanical coupling, i.e. a ‘halo effect’, which may confound segmentation of targeted anatomical structures (Evertsson *et al* 2017). As a first step to address this problem, here we propose a method to more accurately represent the distribution of SPIO contrast agents in homogeneous elastic media that may eventually lead to improved biomedical applicability of MMUS and MMOCT. While the focus of the following article is on an MMUS platform, we expect our findings to be similarly relevant to MMOCT due to the analogous nature of OCT and ultrasonic imaging (Huang *et al* 1991).

Despite the wide variety MMUS hardware implementations and signal processing algorithms, all MMUS systems reported to date operate on displacement fields. No physical model has yet been experimentally demonstrated in imaging the SPIO distribution within a magnetomotive imaging sample that corrects for confounding halo effects surrounding regions of high SPIO density. Clinically, such a model could provide more accurate sizing of targeted anatomical structures such as thrombi or tumor and, in turn, inform prognosis and choice of therapy. For instance, thrombus volume (Parr *et al* 2011, Zhao *et al* 2014) is a relevant parameter in the progression of thromboembolic diseases, as is the size of tumors (Carter *et al* 1989) in survival from breast cancer.

Accurate reconstruction of the SPIO density distribution requires modeling the physical mechanism of magnetomotive imaging contrast, which is a function of both the local

concentration of SPIOs and the local stiffness of the medium (Oldenburg *et al* 2005b, Levy *et al* 2018). Thus, using alternate methods to measure medium stiffness (elastography), one may be able to estimate the true density distribution of SPIOs. As a starting point, here we investigate whether SPIO density distribution may be accurately estimated in a homogeneous, linear, and isotropic elastic medium using MMUS. One challenge is that MMUS conventionally scans displacements only in the axial (perpendicular to the transducer plane) direction and over individual 2D frames with linear array transducers. However, SPIOs existing immediately outside of the 2D frame affect the displacement in-plane. While 3D MMUS would be needed to reconstruct an arbitrary SPIO density distribution, our initial approach is to develop a 2D method using prior assumptions about the out-of-plane SPIO distribution, and to explore the sensitivity of the resulting reconstructions with errors in the priors. In certain imaging scenarios, the method proposed in the following sections may lead to improved SPIO density distribution estimates in 2D MMUS, which is logistically simpler than 3D.

Related prior work was reported by Hossain *et al* (2012), who simulated static displacement fields by finite-element modeling and proposed an inverse method by direct substitution of the displacement field into the governing equation of linear elasticity, the Navier-Cauchy equation. Importantly, the forward model employed in that study was an approximation of the 3D Navier-Cauchy equation by the 2D Poisson's equation to circumvent the lack of knowledge of the lateral (normal to axial, and in the imaging plane) and elevational (out of frame) displacement fields. This approximation produced subtle halo artifacts around regions of force loading, while the direct nature of the method is unlikely to be feasible in noisy, speckled displacement fields. In contrast, we propose a model-based reconstruction of SPIO number density distribution using the 3D Navier-Cauchy equation by effectively reducing the problem to 2D by assumption of a finite extent of the body force distribution in elevation. Using this reconstruction framework, this paper is also the first to perform direct comparisons of both a forward model, which generates displacement fields due to arbitrary force distributions, and an inverse model, which reproduces arbitrary body force distributions from given displacement fields, against experimental MMUS images. These comparisons are accomplished using gel phantoms with SPIO-laden inclusions of known shape. *We hypothesize that inverting displacement fields to reconstruct the body force fields reduces mechanical halo effects and reproduces the dimensions of the inclusion more faithfully*. Corroboration of this hypothesis will provide a first experimental validation that MMUS images can be accurately represented by continuum mechanical models, and that improvement of the estimate of the SPIO density distribution by an inverse method is possible in the presence of speckle and clutter.

Methods

In the following discussion, functions with dependencies only in the coordinates of the imaging plane are indicated by a parallel (∥) superscript and those with dependency in the out-of-plane elevational coordinate are indicated by a perpendicular (⊥) superscript. All symbols and their definitions are listed in the appendix in order of their appearance in the text.

MMUS imaging measures the axial ($\hat{\mathbf{z}}$) component of the displacement field **u** (**r**) (figure 1, right), which designates displacement vectors to all field points **r** within an imaging sample that is deformed due to the application of magnetic gradient forces **f** ($\mathbf{r}_i$) acting on individual SPIOs located at source points $\mathbf{r}_i$. The forces result due to the magnetization of each SPIO in the presence of an external magnetic field **B** (**r**). Here we assume that the magnetic field strengths are sufficiently below the saturation magnetization of the SPIOs such that their magnetization is linear with the applied field, as characterized by their zero-field volume magnetic susceptibility χ_m. We also assume that the time rate of change of the magnetic field is sufficiently small such that the magnetization follows the instantaneous value of the magnetic field; in our experiments the magnetic field waveform has a frequency of ~2 Hz. In a non-magnetic (tissue-like) medium surrounding the SPIOs of permeability μ_0, the force on an SPIO of volume v_n may be written as the well-known magnetic gradient force (Häfeli *et al* 1997):

$$\mathbf{f}(\mathbf{r}_i) = \frac{v_n \chi_m \nabla |\mathbf{B}(\mathbf{r}_i)|^2}{2\mu_0}. \quad (1)$$

In order to consider the summed contribution of all SPIOs, for simplicity we assume that SPIOs are mono-disperse in size and magnetic properties, and that they are sufficiently dilute within the medium such that there is no coupling of magnetization between adjacent particles. In this case, the net force within an imaging pixel of volume v_p can be written as an additive extension of (1):

$$\mathbf{f}(\mathbf{r}) = \zeta(\mathbf{r}) v_p \frac{v_n \chi_m \nabla |\mathbf{B}(\mathbf{r})|^2}{2\mu_0}, \quad (2)$$

where $\zeta(\mathbf{r})$ represents the number density of SPIOs within the pixel centered at position **r**. When discretizing the problem to pixels, the force is distributed over elements of volume and the quantity body force, defined as **b** (**r**) = **f** (**r**) /(ρv_p), becomes relevant, where ρ is the mass density of the medium (Malvern 1969). It is then evident from (2) that the body force distribution within an MMUS sample is directly proportional to the SPIO number density. In fact, if $\nabla |\mathbf{B}|^2$ is uniform throughout the sample, the body force distribution can be taken as a measure of the SPIO number density. This particular importance imparted to the body force distribution provides motivation for the formulation of an inverse model to reconstruct the body force field from the measured displacement field.

The problem of reconstructing the body force field from the 2D axial displacements provided by MMUS has parallels to inverse elastography where the elastic modulus distribution of an imaging sample is derived from the inversion of the measured internal displacement under a known body force field (Doyley 2012). A common approach is to first devise a forward model based on continuum mechanics that models the displacement field of a given sample with a defined modulus distribution, boundary value, and perturbation. Subsequently, an inverse model is formulated by iteratively minimizing a least squares error functional between the measured and modelled displacement, parameterized with respect to

the elastic modulus of interest (Doyley *et al* 1996, Kallel and Bertrand 1996). Here we take an analogous approach to reconstruct the body force distribution from the inversion of the measured displacement field, using a least squares error functional that is now parameterized in terms of the body force distribution, given the displacement field, elastic moduli distributions, and boundary values. Subsequently, a linear preconditioned conjugate gradient solver is employed to iteratively minimize the least squares error functional.

Governing equation of motion

The displacement field of the MMUS imaging sample, assumed to be a linear isotropic elastic material, can be modelled by the static Navier-Cauchy equation (Malvern 1969):

$$\left(\lambda+\mu\right)\nabla\left(\nabla\cdot\mathbf{u}\right)+\mu\nabla^2\mathbf{u}=-\rho\mathbf{b}, \tag{3}$$

where λ and μ are the first and second Lamé parameters, respectively. Although the MMUS apparatus used for this work is a dynamic system with sinusoidally modulated force field, a quasistatic approximation is justified because the driving frequency used in our setup is low (~2 Hz), ensuring that sample deformation occurs on timescales an order of magnitude longer than the elastic wave propagation time. It is estimated that the shear waves travel across the 10 cm wide tissue phantoms of this study within 0.05 s, compared to the 0.5 s period of the driving force. As such, the static displacements and body forces in the model can be equated to the displacement amplitudes and body force amplitudes of the sinusoidal waveforms in the actual experiments. Additionally, we expect that effects of nonlinear elasticity and viscoelasticity are negligible, because a maximum displacement of 100 nm is observed in this work, corresponding to a strain and strain rate of 10^{-6} and $3\times10^{-5}\ \mathrm{s}^{-1}$, respectively.

Forward model

While it appears trivial to solve for the body force distribution through direct substitution of measured displacement into equation (3), we lack lateral and elevational displacement fields to do so with conventional MMUS. Here we employ model-based inversion through the method of Green's function to circumvent the need for these displacement components. The method of Green's function allows one to separately model each component of displacement field **u** (**r**) given the individual component of body forces **b** (**r**) in 3D. Mathematically, this is accomplished by convolving (integrating over source points) the relevant components of the 3 × 3 Green's tensor **G**(**r**) of equation (3) with arbitrary body force distributions and formulating a forward model (de Wit 1960). The Green's tensor can also be tailored to cases with purely axial forces and when displacements outside the imaging plane are not available.

$$\mathbf{u}\left(\mathbf{r}\right)=\mathbf{G}\left(\mathbf{r}\right)*\mathbf{b}\left(\mathbf{r}\right)\Leftrightarrow\tilde{\mathbf{u}}\left(\mathbf{k}\right)=\tilde{\mathbf{G}}\left(\mathbf{k}\right)\tilde{\mathbf{b}}\left(\mathbf{k}\right),\ \text{where} \tag{4}$$

$$\mathbf{G}(\mathbf{r})=\frac{\rho(\lambda+3\mu)}{8\pi\mu(\lambda+2\mu)r}\left[\mathbf{I}-\frac{\lambda+\mu}{\left(\lambda+3\mu\right)r^2}\mathbf{r}\mathbf{r}^T\right]\Leftrightarrow\tilde{\mathbf{G}}(\mathbf{k})=\frac{\rho}{\mu k^2}\left[\mathbf{I}-\frac{\lambda+\mu}{\left(\lambda+2\mu\right)k^2}\mathbf{k}\mathbf{k}^T\right]. \tag{5}$$

We chose to use work in the spatial frequency domain (**k**) for two reasons. First, because the forward model is a convolution, it is computationally convenient to implement it as a multiplication in the Fourier domain. Second, the boundary conditions can be applied more conveniently in the Fourier domain using the method of images, which will be apparent at the end of this subsection. To apply this displacement model to 2D MMUS imaging, we make two additional simplifying approximations. First, the body forces are taken to be purely axial ($\hat{\mathbf{z}}$ component only) as experimental measurements of the magnetic field for our setup in the imaging region reveal that the average axial gradient force field is ~20 times larger than the lateral gradient force field—1.4×10^{-3} T^2 m^{-1} versus 7×10^{-5} T^2 m^{-1}. Secondly, to model the contribution of SPIOs outside of the imaging plane, it is assumed that the body force distribution is uniform in elevation, extending from $-h/2$ to $+h/2$ and centered about the plane of imaging at $y = 0$. In other words, if the SPIOs are confined within a well-defined inclusion, h is the extent of the inclusion in the out-of-plane direction. These assumptions allow the body force and its Fourier transform to be factored into two terms: one explicitly dependent on the elevational coordinate $\left(\mathbf{r}^{\perp} = y\hat{\mathbf{y}}\right)$ and another on the coordinates in the lateral ($\hat{\mathbf{x}}$)/axial($\hat{\mathbf{z}}$) plane of imaging $\left(\mathbf{r}^{\parallel} = x\hat{\mathbf{x}} + z\hat{\mathbf{z}}\right)$ alone, as follows:

$$\mathbf{b}(\mathbf{r}) = b_z(\mathbf{r})\hat{\mathbf{z}} = \mathbf{b}_{\mathbf{z}}^{\parallel}(\mathbf{r}^{\parallel})\mathbf{b}_{\mathbf{z}}^{\perp}(\mathbf{y})\hat{\mathbf{z}}. \tag{6}$$

For the elevation-dependent factor to have the assumed rectangular dependence, its Fourier transform must have a Sinc dependence as follows:

$$b_z^{\perp}(y) = \left[\theta\left(y + \frac{h}{2}\right) - \theta\left(y - \frac{h}{2}\right)\right] \Leftrightarrow \tilde{b}_z^{\perp}\left(k_y\right) = \frac{2\sin\left(\frac{k_y h}{2}\right)}{k_y}, \tag{7}$$

where θ is the Heaviside function. Since MMUS only scans axial displacement, the relevant component of the frequency response from (4), with simplification from (6) becomes

$$\tilde{u}_z(\mathbf{k}) = \tilde{G}_{33}(\mathbf{k})\tilde{b}_z^{\perp}(k_y)\tilde{b}_z^{\parallel}(\mathbf{k}^{\parallel}). \tag{8}$$

The first two factors from (8) can be integrated over $k_y \in [-\infty, \infty]$ and combined into one kernel $\tilde{G}_{33}^{\parallel}\left(\mathbf{k}^{\parallel}\right)$. This reduces the problem to 2D ($\hat{\mathbf{x}}$ and $\hat{\mathbf{z}}$) while encoding the dependence on h over which the SPIOs are assumed to extend in elevation. In the following, we will show how the inversion method is relatively insensitive to values of h above a certain value. The kernel thus becomes:

$$\tilde{G}_{33}^{\parallel}\left(\mathbf{k}^{\parallel}\right)=\frac{2\rho}{\mu}\left[\int_{-\infty}^{\infty}\left[\frac{\sin\left(\frac{k_y h}{2}\right)}{k_y\left(\left(k^{\parallel}\right)^2+k_y^2\right)}\right]dk_y-\frac{\left(\lambda+\mu\right)k_z^2}{\left(\lambda+2\mu\right)}\int_{-\infty}^{\infty}\left[\frac{\sin\left(\frac{k_y h}{2}\right)}{k_y\left(\left(k^{\parallel}\right)^2+k_y^2\right)^2}\right]dk_y\right]$$

$$\tilde{G}_{33}^{\parallel}\left(\mathbf{k}^{\parallel}\right)=\frac{2\pi\rho}{E}\left[\frac{2(1+\nu)}{\left(k^{\parallel}\right)^2}\left(1-e^{-\frac{h}{2}k^{\parallel}}\right)-\frac{(1+\nu)}{(1-\nu)}\frac{k_z^2}{\left(k^{\parallel}\right)^4}\left(1-\left(\frac{2+\frac{h}{2}k^{\parallel}}{2}\right)e^{-\frac{h}{2}k^{\parallel}}\right)\right]. \quad (9)$$

Here, the Young's modulus (E) and Poisson's ratio (ν) have been substituted for λ and μ using the identities: $\lambda = E\nu/(1+\nu)(1-2\nu)$ and $\mu = E/(2(1+\nu))$.

In discretized form, given the spatial distribution of body forces $b_z^{\parallel}\left(\mathbf{r}^{\parallel}\right)$, the axial displacement field $u_z^{\parallel}\left(\mathbf{r}^{\parallel}\right)$ in the imaging plane can be conveniently simulated as a forward operation:

$$u_z^{\parallel}=WF^{\dagger}\tilde{G}_{33}^{\parallel}Fb_z^{\parallel}, \quad (10)$$

where W is a spatial weighting operator, and F, $F^{\dagger}$ are the Fourier and inverse Fourier operators, respectively. The spatial weighting operator W is introduced to assign more importance in the eventual reconstruction to the subspaces of the data that are known more accurately. For simplicity, we choose W to be a binary matrix constructed from intensity-thresholded images where the intensity threshold is set to 40% of the average B-mode US intensity, a level determined in previous work to eliminate pixels with exceedingly high phase noise that mask the underlying displacement signal (Levy *et al* 2018). This effectively removes from the iterative fitting of the inverse model (subsection *C*) pixels for which $u_z^{\parallel}$ are not known. Here, the forward model of (10) is used with experimentally-derived W to model experimental displacement fields, which has the secondary effect of recreating the speckle pattern of the particular dataset from which the filter is derived. It is noted that the displacements of SPIOs, which are on the order of 100 nm for this system (Levy *et al* 2018), are small relative to the US resolution and thus considered to have an insignificant impact on the overall distribution of the body forces.

Importantly, equation (10) allows various realizations of boundary conditions. In our study, however, the hard boundaries of the tissue phantoms are generally far from the imaging region. In phantom-1, for example, the bottom boundary of the mold is located 6 cm below the lower edge of the inclusion while the side boundaries are located 4.5 cm from the nearest edge of the inclusion. In contrast, the transducer-sample interface is located only 1 cm above the top edge of the inclusion. As such, we chose to impose the Dirichlet boundary condition only at the transducer-sample interface: $u_z^{\parallel}\left(x\hat{\mathbf{x}}\right)=0$. This is computationally accomplished by placing an oppositely-directed force distribution across the interface and zero-padding $b_z^{\parallel}$ before applying the forward operation of equation (10). This operation is symbolically

equivalent to imposing the following constraint on the Fourier transform of the body forces, which also ensures that the body forces are real-valued:

$$\tilde{b}_z^{\parallel}(k_x\hat{\mathbf{x}}+k_z\hat{\mathbf{z}}) = -\tilde{b}_z^{\parallel}(k_x\hat{\mathbf{x}}-k_z\hat{\mathbf{z}}) = -\tilde{b}_z^{\parallel}(-k_x\hat{\mathbf{x}}+k_z\hat{\mathbf{z}})^* = \tilde{b}_z^{\parallel}(-k_x\hat{\mathbf{x}}-k_z\hat{\mathbf{z}})^*. \quad (11)$$

Inverse model

An inverse model is employed to reconstruct the body force distribution in the imaging plane given the MMUS-derived axial displacement field, the material parameters (E, ν, and ρ), the assumed thickness h of the SPIO distribution, and the spatial weighing matrix W. The optimal body force distribution b_{opt} can be deduced by minimizing the Thikonov-regularized, weighted least squares error functional constructed from the forward model of (10):

$$b_{opt} = \arg\min\left\{\left\|Wu_z^{\parallel} - WF^{\dagger}\tilde{G}_{33}^{\parallel}Fb_z^{\parallel}\right\|^2 + \gamma\left\|b_z^{\parallel}\right\|^2\right\}, \quad (12)$$

where γ is a regularization parameter chosen via the L-curve method (Hansen 1999). The Euler equation of the least squares error functional, otherwise known as the pseudoinverse, is given by $\left(F^{\dagger}\tilde{G}_{33}^{\parallel}{}^{\dagger}FW^{\dagger}WF^{\dagger}\tilde{G}_{33}^{\parallel}F+\gamma\mathbf{I}\right)b_z^{\parallel} = F^{\dagger}\tilde{G}_{33}^{\parallel}{}^{\dagger}FW^{\dagger}W\,u_z^{\parallel}$. Since $\left(F^{\dagger}\tilde{G}_{33}^{\parallel}{}^{\dagger}FW^{\dagger}WF^{\dagger}\tilde{G}_{33}^{\parallel}F+\gamma\mathbf{I}\right)$ is positive definite symmetric, we employ the well-known conjugate gradient solver (Barrett *et al* 1994) to solve for the body force. A preconditioner of the form $M = F^{\dagger}\left(\tilde{G}_{33}^{\parallel}{}^{\dagger}\tilde{G}_{33}^{\parallel}+\gamma\mathbf{I}\right)$ is used to speed up the iterations.

Sample preparation and data acquisition

Experiential testing of the reconstruction algorithm presented in the previous section was performed on two gelatin phantoms that mimic the mechano-acoustic properties of soft tissue with SPIO-laden inclusions. Each phantom was designed with physiologically relevant material parameters as prescribed by Madsen *et al* (1978) and Hall *et al* (1997), in the range of many types of soft tissue: $\nu \sim 0.5$, $E = 1$ kPa^{-1} MPa, $\rho = 1000$ kg m^{-3}, speed of sound = 1540 m s^{-1}, and frequency dependent attenuation coefficient = 0.3 dB/cm/MHz. Phantom-1 was prepared in an 8 cm × 10 cm × 5 cm (axial-lateral-elevational) rectangular acrylic mold similar to the one described in Levy *et al* (2018), but with different dimensions and without embedded tubing; briefly, the mold has four 0.64 mm diameter low magnetic susceptibility alloy-510 phosphor bronze wires to serve as fiducial markers for outlining the boundaries of the SPIO-laden inclusion. The markers are visible only in the B-mode image, as seen in figure 1. Phantom-2 was prepared in a cylindrical mold 8 cm tall and 7.5 cm in diameter with a slit on the sidewall to facilitate imaging, allowing a variation in inclusion geometry not possible in our custom-built acrylic mold.

Gelatin tissue-mimicking phantoms were prepared in accordance with section II-C of Levy *et al* (2018). The same 5 kPa Young's modulus background material described in this previous work was used for both phantoms 1 and 2, while the inclusions varied slightly. Phantom-1 contained the same 1 cm cubic inclusion geometry, but with an iron (II, III) oxide nanopowder concentration of 4.4 mg Fe ml^{-1}, while phantom-2 was created with a 5

mm × 5 mm × 40 mm (axial-lateral-elevational) inclusion containing 5 mg Fe ml^{-1}. All other parameters were unchanged.

Data on the two tissue-mimicking phantoms was acquired using the open-air MMUS system (figure 1) previously described in detail by Levy *et al* (2018) and Pope *et al* (2013). The system consisted of the Ultrasonix Sonix-Touch scanner with an L14–5/38 linear array transducer (Analogic Corporation, Peabody, MA) that was used to acquire ultrasound RF data at a frame rate of 61.667 frames per second (fps), a center frequency of 10 MHz (fundamental frequency imaging), 70% bandwidth, a 17.5 mm focal depth, and transmit and receive f-numbers of 1.2 and 1.8, respectively. The transducer was centered beneath a pair of solenoid electromagnets in an antiparallel configuration with grain-oriented electrical steel cores. Since the magnetic gradient force scales quadratically with the driving voltage (Oldenburg *et al* 2008), the waveform generator was modulated with a square root sinusoidal signal to generate a 2 Hz sinusoidal force in the imaging region (Levy *et al* 2018).

During data acquisition, seven datasets were collected for phantom-1 and two for phantom-2. Each set consisted of two 7.5 s image stacks of beamformed RF data, one collected with the magnetic field modulated and another with the magnetic field off for background subtraction. Each frame consists of 46 A-lines and is sampled into 255 pixels across 3.8 cm, laterally, and into 1568 pixels spanning 2.95 cm, axially. The RF data was processed offline with our previously published frequency and phase locking (FPL) algorithm (Pope *et al* 2013) to render the axial displacement field. Briefly, RF data was Hilbert transformed, its argument (phase) extracted, and the temporal differential phase computed. Then, the Fourier component of the differential phase at the magnet driving frequency (2 Hz) was computed; the phase of this Fourier component was used as part of a cosine filter to select motion only in-phase with the oscillating magnetic field, which weighted the magnitude of the Fourier component with a value between 0 and 1. This frequency-and-phase-filtered signal was converted to a vibrational displacement amplitude based upon calibration through the discrete Fourier transform. Finally, an intensity threshold filter, described in detail in the *Forward Model* subsection, was applied to the frequency-and-phase-filtered displacement and a median filter with box size nominally 3 times the resolution was used for speckle suppression. All post-processing was performed in MATLAB (Mathworks Inc, Natick, MA).

Simulation-based testing of inverse method robustness

Reconstruction of the body forces from the proposed method of inversion of MMUS displacement fields requires knowledge of the kernel $\tilde{G}^{\parallel}_{33}$ given by equation (9). Since $\tilde{G}^{\parallel}_{33}$ is a function of sample parameters ρ, E, ν, and h, it is advantageous to know the effect of their uncertainties in the robustness of the inversion. Furthermore, reconstructions may be susceptible to the noise level of the displacement fields themselves. To investigate these effects, a displacement field was simulated by the forward model given by equation (10) with well-defined sample parameters ρ, E, ν, h, a rectangular body force distribution b_0, a uniform spatial weighting matrix ($W = \mathbf{I}$), and an additive Gaussian noise of varying signal to noise ratio (SNR). The body force distribution b_0 was created as a 1568 × 255, 2.9 cm × 3.8 cm binary image (same size as experimental images) with ones inside a 1 cm × 1 cm

rectangular window and zeroes outside. To investigate the effect of a particular sample parameter, the displacement field was then inverted assuming the same values for the sample parameters used in simulating the displacement field, but with a difference for the particular parameter under investigation. For each parameter in question, a range of values around the true value of the parameter was investigated in a series of inversions for each of which a 2D correlation coefficient with the known body force distribution b_0 was calculated and plotted against the guess parameter value. Similarly, to study the effect of SNR alone on inversion, a series of Gaussian noises in the range 0–20 dB were added to the displacement field and inverted with the exact kernel used for simulation. The 2D correlation coefficient with the known body force distribution was then plotted against the corresponding displacement field SNRs.

Performance evaluation metrics

To quantify the accuracy and efficacy of the model-based inversions compared to raw displacement field measurements (traditional MMUS), three standard metrics were considered. The first of the metrics, contrast-to-noise ratio, is calculated as: $\mathrm{CNR} = \left(\left\langle u_{in}\right\rangle - \left\langle u_{\mathrm{out}}\right\rangle\right)/\sqrt{\left\langle u_{\mathrm{out}}\right\rangle^2 - \left\langle u_{\mathrm{out}}^2\right\rangle}$, where u_{in} refers to signal inside the inclusion, u_{out} refers to the signal in the background, and the angular brackets represent the mean value of the argument. The background was chosen to be a rectangular annulus surrounding the inclusion with an area three times that of the inclusion, and a rectangular exterior bounded with a diagonal two times that of the inclusion. This choice was made instead of the entire background to capture motion artifacts which are more prevalent closer to the inclusion, in all directions.

The inclusion height and width derived from the MMUS images, in comparison to the *a priori* inclusion dimensions, were also calculated as performance metrics. The process of calculating inclusion height involved taking columns within the lateral extent of the inclusion and individually calculating their normalized cross-correlation coefficients with an ensemble of rectangular functions of varying window sizes, incremented one pixel a time. For each column, the best-fit rectangular distribution was taken to be that from the ensemble which had the maximum correlation coefficient. Ultimately, inclusion height was defined as the median of the window sizes of all best-fit rectangular distributions. The advantages of using this method are that possible shifts of the inclusion position from the presumed boundary are accounted for by using cross-correlation, and normalization of the cross-correlation coefficient disambiguates the scaling of the ensemble of rectangular distributions. A similar process was used to calculate inclusion width by taking rows within the axial extent of the inclusion.

Results

Robustness of inversion algorithm to input parameters

The robustness of the inversion algorithm to uncertainties in sample parameters ρ, E, ν, h and the displacement field SNR is depicted in figure 2. As expected, for each of the cases of ρ, E, h, and ν, the inverted images exhibit maximum correlation with the body force distribution at the value of the parameter used in the forward model. Importantly, even when

the parameters used in the inversion are highly deviated from the true values, the inversions exhibit higher correlation with the body force distribution than do the displacement fields themselves (dashed horizontal or curved, in figure 2(c)), except in the case of severe under-estimation of E (figure 2(b)). Nevertheless, at values of E larger than the true value, the correlations decrease at a slow rate, suggesting high stability when overestimating E in the reconstructions. The robustness spectrum of h (figure 2(d)) follows a similar pattern to that of E with a steep decrease in the correlation coefficient at values smaller than the true h and a gradual roll-off at values larger than the true h. For mass density ρ, the inversion method presented here is quite robust in the 500–1500 kg m^{-3} range. As tissue and tissue-mimicking phantoms generally have densities similar to that of water, this range is likely to be sufficient for all practical biological purposes. Lastly, the robustness spectrum of both v (figure 2(c)) and SNR (figure 2(e)) show a monotonic increase with respect to the parameter in question, with correlation values of the reconstructions always greater than that of the displacement field itself. The Poisson's ratio of gel phantoms, as well as soft tissues, are close to the maximum value of 0.5 due to their nearly incompressible nature. However, the SNR of MMUS displacement fields can vary widely depending on the SPIO concentration and the hardware-specific ability of the imaging system to reject external noise. For the open-air MMUS setup used in our study, SNRs ranging from 0.8–7.6 dB have been reported (Pope *et al* 2013).

Inversion applied to experimentally-acquired MMUS displacement fields

Seven displacement fields of phantom-1 and two of phantom-2 were inverted using the model-based inversion of equation (12). Additionally, for each experimentally-obtained MMUS displacement field, a corresponding field was simulated according to the forward model of equation (10) using the sample parameters (ρ, E, v, h), SNR determined from the MMUS signal inside the inclusion, a uniform body force distribution as discerned from the inclusion location via the fiducial markers, and the intensity threshold filter W from the B-mode image. The simulated displacement fields were then inverted using the same model-based inversion. Figures 3(a)–(d) is a side-by-side presentation of the resulting images from the fourth of the seven chronologically-acquired datasets from phantom 1. Likewise, figures 3(e)–(h) is a side-by-side presentation of the same exercise on a representative phantom-2 dataset. Signals halfway within the inclusion bounds were also sampled both axially and laterally from the MMUS and simulated displacement fields. These samples are plotted as signal versus depth/width curves and overlaid with their corresponding samples from the inversions and presented in figures 3(i)–(l) for the phantom-1 dataset and in figures 3(m)–(p) for the phantom-2 dataset for which the fields are displayed.

Qualitatively, the halos surrounding inclusion boundaries are seen to be reduced in the inversions of simulated and experimental displacement fields in both the representative phantom-1 and phantom-2 datasets. This effect is further substantiated by the bar chart in figure 4, which presents the mean CNR, inclusion height, and inclusion width of the experimental and simulated displacement fields and their inversions of all acquired datasets of phantom-1 ($N = 7$) and phantom-2 ($N = 2$). For both phantoms, mean CNR of the field inversions are larger than that of the fields themselves, whereas mean inclusion height and width of the field inversions are closer to the true value than are the corresponding metrics

from the displacement fields. These observations, specifically of phantom-1, are found to be significant ($p = 0.0078$) under one-tailed Wilcoxon signed-rank tests at a 5% significance level in all three metrics. It is also notable that differences in sample mean of all metrics between MMUS and simulated displacement fields are not statistically significant for phantom-1, highlighting the accuracy of the forward model. Two-tailed Wilcoxon rank-sum tests fail to reject the null hypotheses at 5% significant level with $p = 1.00$ for CNR, $p = 0.10$ for height, and $p = 0.38$ for width. Due to its limited sample size, such statistical analyses is not preformed for phantom-2.

Discussion

Here we develop and validate a physical model of elastic sample deformation in response to an internal body force field. Given the assumptions used in the development of equation (2), we posit that the proportionality between the body force field and the SPIO density distribution can be exploited to reduce the halo effect in MMUS imaging. This is confirmed by comparing the *a priori* SPIO density distribution in our phantoms with the body force distribution obtained from inverting the experimental displacement data, resulting in a qualitative reduction of halo effects in post-inversion images of figure 3. Added confirmation is provided by comparing the forward model-predicted displacements from the *a priori* SPIO distribution, against the actual displacements, as simulated displacement fields lacked statistically significant difference in the performance metrics: CNR, inclusion height, and width. Importantly, this allows the inverse method to be used as a signal processing tool to improve the estimates of the true, underlying SPIO distribution, which is observed as an increase in CNR, a better match of the inclusion dimensions with the true dimensions, and a qualitative improvement in the image fidelity (i.e. reduction of the halo).

Specifically, the increase in CNR in both the experimental and simulated data of phantom-1 and 2 upon inversion is indicative of the strength of the algorithm to reject motion artifacts and enhance the detectability of the inclusion. It should be pointed out that the small differences in CNR increase between the experimental and simulated data is attributed to boundary value fidelity of the inversions. Because inversions of experimental displacement fields only approximate the boundary condition as a zero-displacement constraint on the sample-transducer boundary, the CNR increase is low compared to inversions of simulated displacement fields which exactly replicate the boundary condition used in the simulations. This limiting assumption is necessary for a generalized application of our inversion scheme to diverse MMUS samples where the only universal boundary condition is the zero-displacement constraint at the sample-transducer interface. We believe that these assumptions are fairly agnostic for *in vivo* applications and will introduce minimal error in the reconstructions unless there are hard boundaries near the volume being probed.

Likewise, the improved accuracy of the measured dimensions of the inclusions in post-inversion suggest that this method can aid in delineating the shape and boundary of an SPIO labelled structure. Average percent error in inclusion height and width of phantom-1 MMUS displacement fields went down from 195% ± 18% and 151% ± 13% to 9.68% ± 1.3% and 4.95% ± 4.8%, respectively, post-inversion. Likewise, average percent error in inclusion height and width of phantom-2 MMUS displacement fields went down from 282% ± 1% and

53.7% ± 1.5% to 20.0% ± 8.0% and −14.8% ± 1.6%, respectively, post-inversion. The percent errors here in inclusion height are consistently larger than the percent errors in inclusion width. This points to the directional bias of the extent of motion artifacts, namely, that motion artifacts are more pronounced axially than they are laterally.

A natural extension of this work is to accommodate inversions of 3D displacement fields of inhomogeneous and anisotropic samples. While the model-based inversion presented here is effectively 2D, it tracks elevational contributions to displacement fields by assuming a well-defined thickness of SPIO density distribution centered about the transducer. These assumptions are not necessary if high resolution 3D data can be obtained via either scanning of our existing US probe in elevation, or using a US 2D matrix array transducer (Szabo and Lewin 2013). To extend the method for application in elastically inhomogeneous and/or anisotropic samples, established US-based elastography techniques, such as quasistatic (Ophir *et al* 1991), harmonic (Parker *et al* 1990), or transient (Sarvazyan *et al* 1998) elastography, could be used to first estimate the relevant elastic moduli of samples before performing MMUS scans. Then, the proposed inversion method could be applied by solving for a new Green's tensor of the modified equations of motion that account for inhomogeneity and anisotropy (Tonon *et al* 2001).

Further, the inversion scheme presented in this work may be executed with other implementations of motion detection algorithms and hardware in the future. Inversion can be applied to displacement fields generated through Doppler (Oh *et al* 2006), cross-correlation (Mehrmohammadi *et al* 2007), and blind source separation-based FPL (Hossain *et al* 2018) methods, among others. Inversion can also be applied to systems where varying waveforms for temporal modulation of the magnetic gradient force are used, including pulsed (Mehrmohammadi *et al* 2009) or coded (Fink *et al* 2017), to the extent that the rendered image signals are linear with respect to the displacement field. Finally, inversion can be applied equally effectively to displacement fields collected from MMOCT.

Conclusion

Artifacts in MMUS are inherent because the system is premised on motion detection, which captures an integrated and continuous displacement field surrounding individual SPIOs, manifested due to their mechanical coupling with the sample. In this work we first model these artifacts by the quasistatic solution of the Navier-Cauchy equation, and then under the assumption that the force field is uniform in the elevational plane, reduce it to a 2D problem. We then propose a reconstruction of the body forces, which are proportional to the underlying SPIO density distribution under certain assumptions, given the displacement field and some material parameters. The reconstruction algorithm is a preconditioned, regularized, weighted conjugate gradient iterative solver. Reconstruction is shown to be robust to a range of uncertainties in the parameters ρ, E, h, and ν necessary to generate the forward kernel, as well as a wide range of input displacement field SNRs. Reconstruction is tested on MMUS images of two gelatin inclusion tissue phantoms and is shown to increase the CNR of both the experimental displacement field and their simulated counterparts. Reconstruction also renders the dimensions of the SPIO-laden inclusion closer to the true values than does the conventional displacement field alone. These results indicate that our

proposed model-based inversion of MMUS displacement fields can be used as a signal processing tool, in addition to its utility in characterizing the SPIO distribution within linear, isotropic, and elastically homogeneous MMUS samples.

Acknowledgment

D Thapa would like to thank Md Murad Hossain of the Biomedical Engineering department at the University of North Carolina, Chapel Hill, USA for his guidance in this study. This study was funded by the National Institutes of Health (R21 HL 119928) and the U.S. Department of Defense (FA9550-14-1-0208 and N00014-10-1-0792).

Appendix.: List of mathematical symbols in order of their appearance in the text

$\hat{\mathbf{z}}$	Unit vector along axial direction
$\mathbf{u}$	3D displacement field vector within the imaging sample
$\mathbf{r}$	3D position vector within the imaging sample
$\mathbf{f}$	3D magnetic gradient force
$\mathbf{r}_i$	3D position vector of the ith SPIO
$\mathbf{B}$	3D magnetic field vector
χ_m	Magnetic susceptibility of the MNPs
μ_0	Permeability of free space
v_n	Volume of an SPIO
v_p	Volume of an MMUS pixel
ζ	SPIO number density distribution
$\mathbf{b}$	3D body force vector
ρ	Mass density
λ	Lamé's first parameter
μ	Lamé's second parameter, also the shear modulus
$\mathbf{G}$	Green's tensor of the Navier-Cauchy equation
$\widetilde{\mathbf{u}}$	Fourier transform of the 3D displacement field vector within the imaging sample
$\widetilde{\mathbf{G}}$	Fourier transform of the Green's tensor of the Navier-Cauchy equation
$\widetilde{\mathbf{b}}$	Fourier transforms of the 3D body force vector
$\mathbf{k}$	Spatial frequency vector
$\mathbf{I}$	Identity matrix
$\mathbf{r}^T$	Transpose of the position vector
$\mathbf{k}^T$	Transpose of the frequency vector
r	Magnitude of position vector
k	Magnitude of the frequency vector
h	The extent of SPIO-laden inclusion in the out-of-plane direction
y	Out-of-plane component of the position vector
$\mathbf{r}^{\perp}$	Position vector in the out of plane direction
$\mathbf{r}^{\parallel}$	Position vector in the plane of imaging
$\hat{\mathbf{x}}$	Unit vector along lateral direction
$\hat{\mathbf{y}}$	Unit vector along elevational direction

b_z	Axial component of the body force
$b_z^{\parallel}$	In-plane factor of the axial body force
$b_z^{\perp}$	Out-of-plane factor of the axial body force
θ	Heaviside step function
$\tilde{b}_z^{\perp}$	Fourier transform of the out-of-plane factor of the axial body force
k_y	Out-of-plane component of the spatial frequency vector
$\tilde{u}_z$	Fourier transform of the axial displacement field
$\tilde{G}_{33}$	Fourier transform of the 33 component of the Green's tensor
$\mathbf{k}^{\parallel}$	Spatial frequency vector in the plane of imaging
$\tilde{G}_{33}^{\parallel}$	Fourier transform of the 33 component of the Green's tensor modified for use in 2D
$k^{\parallel}$	Magnitude of the spatial frequency vector in the plane of imaging
E	Young's modulus of imaging sample
v	Poisson's ratio of imaging sample
$u_z^{\parallel}$	The in-plane axial displacement field
F	Fourier transform operator
$F^{\dagger}$	Inverse or complex conjugate transpose of the Fourier transform operator
W	Spatial weighting operator
$\tilde{b}_z^{\parallel}$	Fourier transform of the in-plane factor of the axial body force
b_{opt}	Body force distribution obtained from optimization
γ	Regularization parameter
$\tilde{G}_{33}^{\parallel\ \dagger}$	Complex conjugate transpose of the forward model kernel
$W^{\dagger}$	Complex conjugate transpose of the spatial weighing matrix
M	Preconditioner for conjugate gradient solver
b_0	Rectangular body force distribution for simulating displacement field in robustness test

References

Barrett R, Berry M, Chan TF, Demmel J, Donato J, Dongarra J, Eijkhout V, Pozo R, Romine C and van der Vorst H 1994 Templates for the solution of linear systems (Philadelphia: SIAM) pp 14–7

Carter CL, Allen C and Henson DE 1989 Relation of tumor size, lymph node status, and survival in 24740 breast cancer cases Cancer 63 181–7 [PubMed: 2910416]

de Wit R 1960 The continuum theory of stationary dislocations Solid State Phys. 10 249–92

Doyley MM. 2012; Model-based elastography: a survey of approaches to the inverse elasticity problem. Phys. Med. Biol. 57:R35. [PubMed: 22222839]

Doyley M, Bamber J, Shiina T and Leach M 1996 Reconstruction of elastic modulus distribution from envelope detected B-mode data 1996 IEEE Ultrasonics Symp. Proc 2 1611–4

Evertsson M. et al. 2017; Combined magnetomotive ultrasound, PET/CT, and MR imaging of ^{68}Ga-labelled superparamagnetic iron oxide nanoparticles in rat sentinel lymph nodes in vivo. Sci. Rep. 7:4824. [PubMed: 28684867]

Evertsson M, Kjellman P, Cinthio M, Fredriksson S, Zandt R I t, Persson HWand Jansson T 2014 Multimodal detection of iron oxide nanoparticles in rat lymph nodes using magnetomotive

ultrasound imaging and magnetic resonance imaging IEEE Trans. Ultrason. Ferroelectr. Freq. Control 61 1276–83 [PubMed: 25073135]

Fink M, Ermert H, Lyer S and Alexiou C 2017 Influence of naturally occurring tissue movements on magnetomotive ultrasound detection of iron oxide nanoparticles for magnetic drug targeting 2017 IEEE Int. Ultrasonics Symp. (IUS) pp 1–6

Häfeli U, Schüt W and Teller J 1997 Scientific and Clinical Applications of Magnetic Carriers (New York: Plenum) pp 220–1

Hall T, Bilgen M, Insana M and Krouskop T 1997 Phantom materials for elastography IEEE Trans. Ultrason. Ferroelectr. Freq. Control 44 1355–65

Hansen PC 1999 The L-curve and Its Use in the Numerical Treatment of Inverse Problems (Lyngby: IMM, Department of Mathematical Modelling, Technical University of Denmark)

Hossain A, Cho M and Lee S 2012 Magnetic nanoparticle density mapping from the magnetically induced displacement data: a simulation study Biomed. Eng. Online 11 11 [PubMed: 22394477]

Hossain MM, Levy BE, Thapa D, Oldenburg AL and Gallippi CM 2018 Blind source separation-based motion detector for imaging superparamagnetic iron oxide (SPIO) particles in magnetomotive ultrasound imaging IEEE Trans. Med. Imaging 37 2356–66 [PubMed: 29994656]

Huang D et al. 1991 Optical coherence tomography Science 254 1178–81 [PubMed: 1957169]

John R, Rezaeipoor R, Adie SG, Chaney EJ, Oldenburg AL, Marjanovic M, Haldar JP, Sutton BP and Boppart SA 2010 In vivo magnetomotive optical molecular imaging using targeted magnetic nanoprobes Proc. Natl Acad. Sci 107 8085–90 [PubMed: 20404194]

Kallel F and Bertrand M 1996 Tissue elasticity reconstruction using linear perturbation method IEEE Trans. Med. Imaging 15 299–313 [PubMed: 18215911]

Kim J, Ahmad A, Li J, Marjanovic M, Chaney EJ, Suslick KS and Boppart SA 2016 Intravascular magnetomotive optical coherence tomography of targeted early-stage atherosclerotic changes in ex vivo hyperlipidemic rabbit aortas J. Biophotonics 9 109–16 [PubMed: 25688525]

Levy BE, Hossain MM, Sierchio JM, Thapa D, Gallippi CM and Oldenburg AL 2018 Effect of model thrombus volume and elastic modulus on magnetomotive ultrasound signal under pulsatile flow IEEE Trans. Ultrason. Ferroelectr. Freq. Control 65 1380–8 [PubMed: 29993541]

Madsen EL, Zagzebski JA, Banjavie RA and Jutila RE 1978 Tissue mimicking materials for ultrasound phantoms Med. Phys 5 391–4 [PubMed: 713972]

Malvern LE 1969 Introduction to the Mechanics of a Continuous Medium (Englewood Cliffs, NJ: Prentice-Hall) pp 497–504

Mehrmohammadi M et al. 2007 Imaging of iron oxide nanoparticles using magneto-motive ultrasound 2007 IEEE Ultrasonics Symp. Proc pp 652–5

Mehrmohammadi M, Oh J, Aglyamov S, Karpiouk A and Emelianov S 2009 Pulsed magneto-acoustic imaging 2009 Annual Int. Conf. of the IEEE Engineering in Medicine and Biology Society pp 4771–4

Oh J, Feldman MD, Kim J, Condit C, Emelianov S and Milner TE 2006 Detection of magnetic nanoparticles in tissue using magneto-motive ultrasound Nanotechnology 17 4183–90 [PubMed: 21727557]

Oldenburg AL, Crecea V, Rinne SA and Boppart SA 2008 Phase-resolved magnetomotive OCT for imaging nanomolar concentrations of magnetic nanoparticles in tissues Opt. Express 16 11525–39 [PubMed: 18648474]

Oldenburg AL, Gunther JR and Boppart SA 2005a Imaging magnetically labeled cells with magnetomotive optical coherence tomography Opt. Lett 30 747 [PubMed: 15832926]

Oldenburg AL, Toublan FJ-J, Suslick KS, Wei A and Boppart SA 2005b Magnetomotive contrast for in vivo optical coherence tomography Opt. Express 13 6597 [PubMed: 19498675]

Ophir J, Céspedes I, Ponnekanti H, Yazdi Y and Li X 1991 Elastography: a quantitative method for imaging the elasticity of biological tissues Ultrason. Imaging 13 111–34

Parker K, Huang S, Musulin R and Lerner R 1990 Tissue response to mechanical vibrations for ‘sonoelasticity imaging’ Ultrasound Med. Biol 16 241–6 [PubMed: 2194336]

Parr A, Mccann M, Bradshaw B, Shahzad A, Buttner P and Golledge J 2011 Thrombus volume is associated with cardiovascular events and aneurysm growth in patients who have abdominal aortic aneurysms J. Vascular Surg 53 28–35

Pope AG, Wu G, Mcwhorter FY, Merricks EP, Nichols TC, Czernuszewicz TJ, Gallippi CM and Oldenburg AL 2013 Contrast-enhanced imaging of SPIO-labeled platelets using magnetomotive ultrasound Phys. Med. Biol 58 7277–90 [PubMed: 24077004]

Sarvazyan AP, Rudenko OV, Swanson SD, Fowlkes J and Emelianov SY 1998 Shear wave elasticity imaging: a new ultrasonic technology of medical diagnostics Ultrasound Med. Biol 24 1419–35 [PubMed: 10385964]

Szabo TL and Lewin PA 2013 Ultrasound transducer selection in clinical imaging practice J. Ultrasound Med 32 573–82 [PubMed: 23525382]

Tonon F, Pan E and Amadei B 2001 Green's functions and boundary element method formulation for 3D anisotropic media Comput. Struct 79 469–82

Zhao L, Prior SJ, Kampmann M, Sorkin JD, Caldwell K, Braganza M, Mcevoy S and Lal BK 2014 Measurement of thrombus resolution using three-dimensional ultrasound assessment of deep vein thrombosis volume J. Vascular Surg 2 140–7

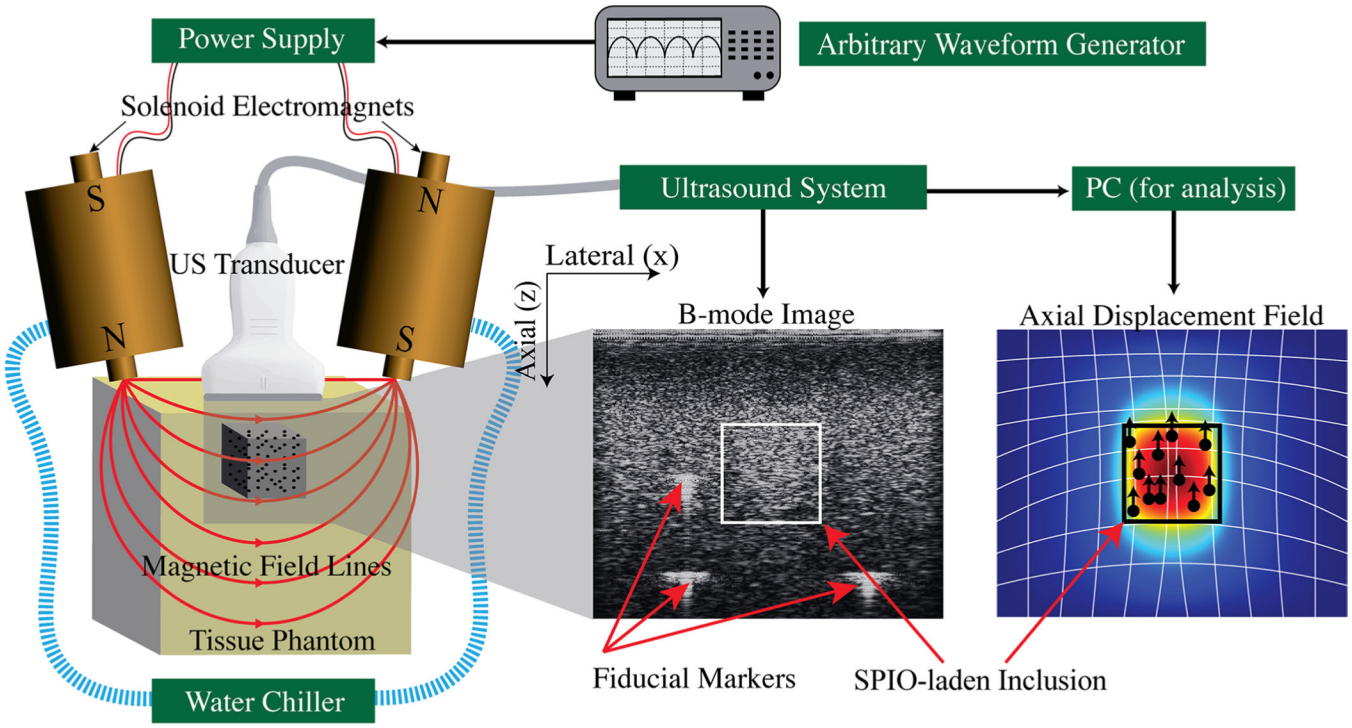

Figure 1.

Schematic of the open-air MMUS system and how it generates displacement fields. Left-a tissue phantom with SPIO-laden inclusion is imaged by the open-air MMUS system. Middle-structural US image (B-mode) of the phantom with visible fiducial markers that aid in outlining the inclusion boundary from the known design of the phantom mold. Right-magnetic gradient field exerts body forces predominantly in the axial direction causing internal displacements (concept color map) in the sample that extend beyond the boundaries of the inclusion. Gridlines, which were squares in pre-loading, are added to show the overall displacement of the nodes under stress.

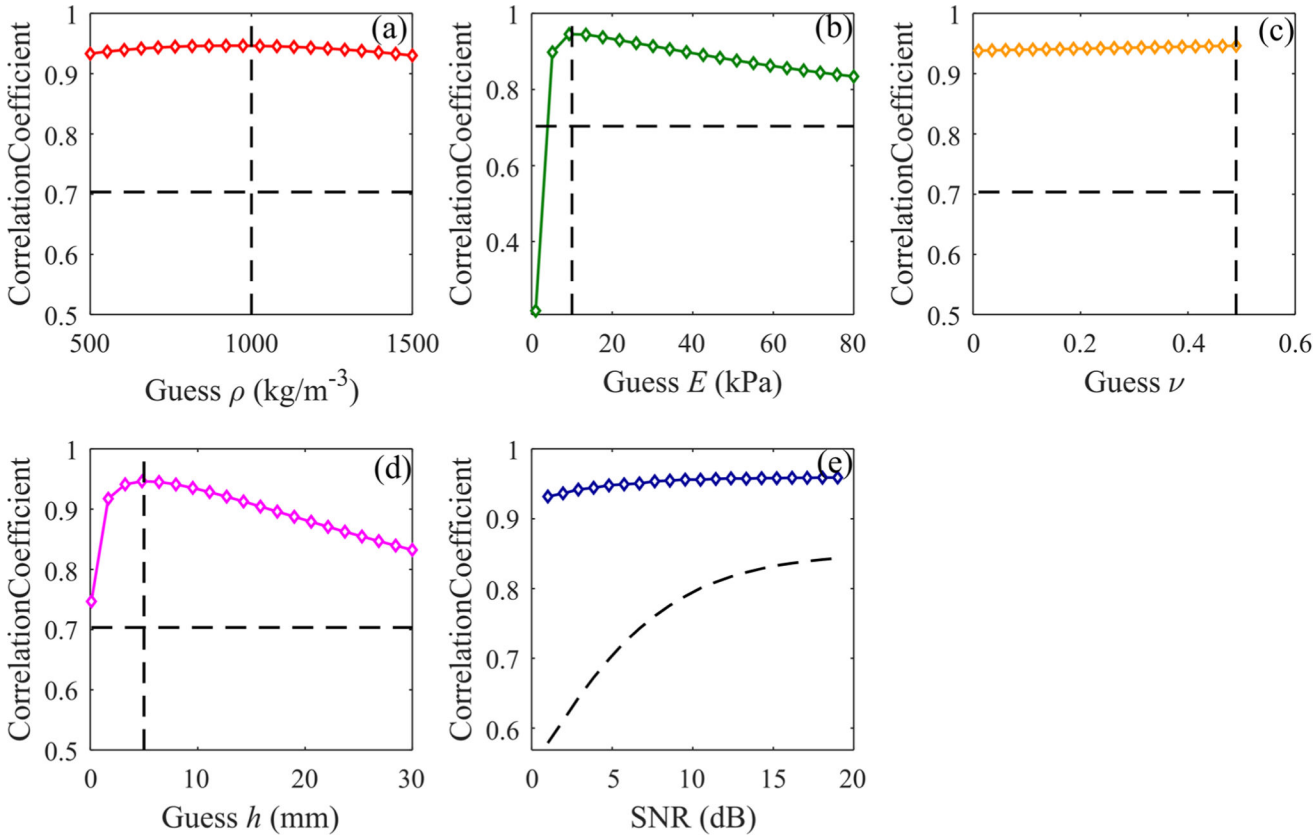

Figure 2.

Robustness of the inverse method to sample parameters (ρ, E, ν, h) and image SNR measured in terms of the correlation with the known body force distribution. Inversion is applied to a displacement field simulated using $\rho = 1000$ kgm^{-3}, $E = 10$ kPa, $\nu = 0.49$, $h = 5$ mm, and SNR = 5 dB, by assuming variations only in ρ in (a), E in (b), ν in (c), and h in (d) while keeping other parameters true to simulation. In (e) inversions are applied on displacement fields of varying SNRs with all parameters true to simulation. Dashed vertical lines represent the parameter value used in simulation while dashed horizontal or curved, in (e), lines represent the normalized 2D correlation coefficient between the body force distribution and the displacement field before performing the inversion, to be taken as a baseline.

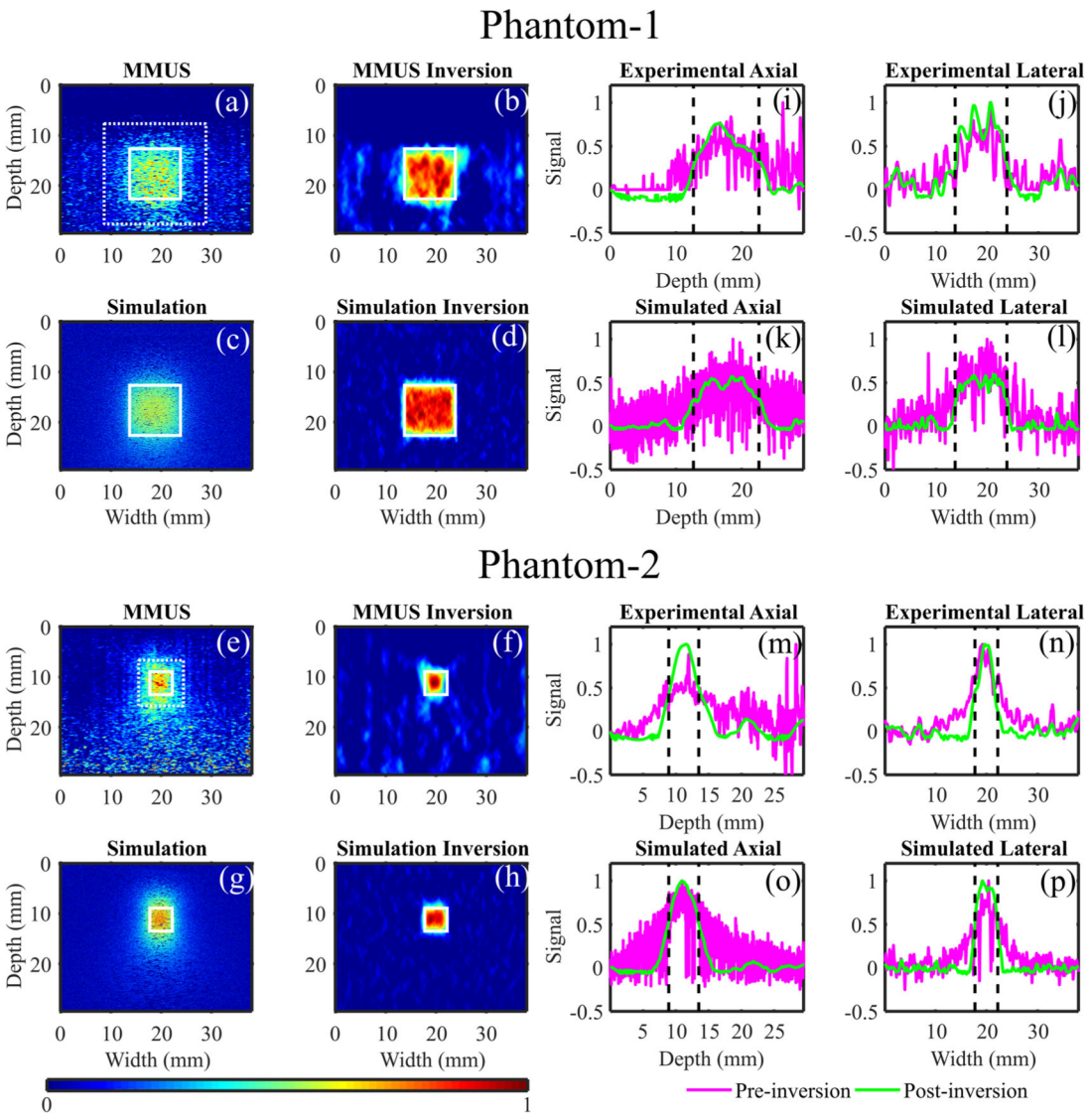

Figure 3.

Displacement fields (a), (c), (e) and (g) and corresponding body force distributions (b), (d), (f) and (h) rendered from inversion of experimental data (a) and (e) and their simulations (c) and (g) using the forward model. The solid boxes outline inclusion boundary ascertained by comparison with the CAD model used to design the phantom mold, while the dashed exterior boxes in (a) and (e) outline the extent of the image background considered for CNR calculations. Also shown are image columns sampled axially (i), (k), (m) and (o) and rows sampled laterally (j), (l), (n) and (p) about the center of the inclusion to aid in visualizing the extent of the inclusion. The dashed vertical lines represent the known bounds of the inclusion. Panels (a)–(d) and (i)–(l) correspond to images and plots from phantom-1 while panels (e)–(h) and (m)–(p) correspond to those from phantom-2. For consistency, all colormaps are scaled from 0 to 1 with 1 representing the maximum pixel value and all negative pixels being mapped to 0.

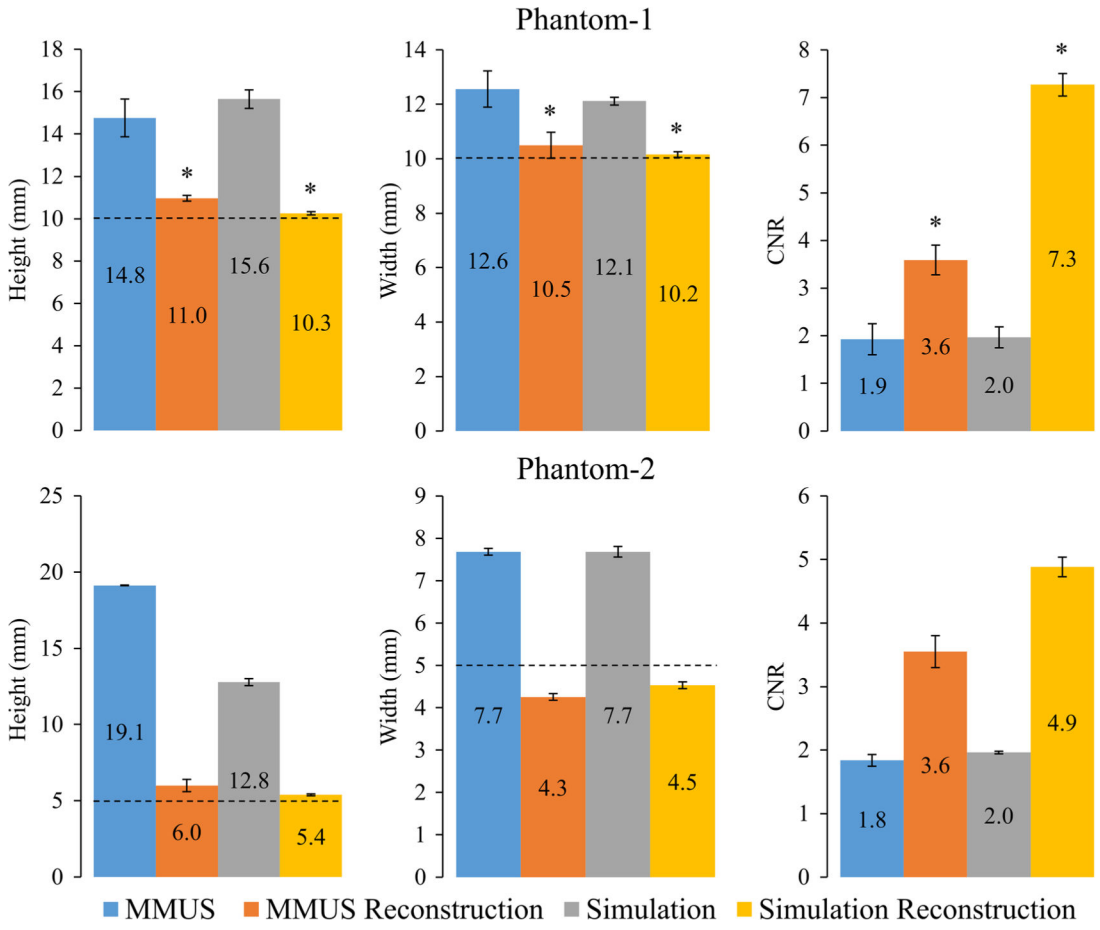

Figure 4.

Summary of the results of inversion on MMUS-rendered displacement fields and simulations together with their respective inversions for phantom-1 (top row) and phantom-2 (bottom row). Results are categorized by image metrics: inclusion height (left), inclusion width (center), and CNR (right). Dashed horizontal lines represent the true dimensions of the inclusions. Data labels display mean value of the ensembles, $N = 7$ for phantom-1 and $N = 2$ for phantom-2. Error bars are plotted as standard deviation of the samples. Where error bars are not visually discernible, they are too small to be presented in the same scale as the sample means. *symbolizes $p < 0.01$ for pre-inversion versus post-inversion metrics.